

Chapter 4

Observations and Data Reduction

4.1 The Objects

The objects studied in this thesis were the three bright, radio-quiet QSOs 2206–199N, 1101–264, and 2348–147.

Details of the objects observed are given in Table 4.1.

4.2 Echelle Observations

All of the high resolution observations used in this thesis were made at the 3.9 m Anglo-Australian Telescope (AAT), at Siding Spring Observatory, near the town of Coonabarabran, New South Wales. The high resolution spectra were taken with the University College London Echelle Spectrograph (UCLES) (Walker and Diego, 1985; Robinson *et al.*, 1989) at the f/36 coudé focus of the telescope and the Image Photon Counting System (IPCS) detector (Lucey and Taylor, 1983).

Details of the observations are given in Table 4.2.

4.2.1 Description of Observations

This Section describes the observing procedures used to obtain the echelle spectra of the target QSOs.

Spectrograph Configuration

The 79 grooves mm^{-1} echelle grating of UCLES was used for all of the observations. The cross-dispersing prisms of the spectrograph spread the echelle orders over several millimetres in the detector plane. An echellogram, showing the positions of the cross-dispersed orders, is shown in Figure 4.1. A 31.6 grooves mm^{-1} grating is also available, but it produces spectral orders 2.5 times closer together, which does not allow adequate recording of the sky (see below).

Table 4.1 List of QSOs observed, showing the object names, emission redshifts, blue magnitudes, and other references.

Object	z_{em}	B	References
Q1101–264	2.147	16.08	Osmer and Smith (1977) Carswell <i>et al.</i> (1982) Carswell <i>et al.</i> (1984) Boissé and Bergeron (1985) Petitjean and Bergeron (1990) Carswell <i>et al.</i> (1991) (CLPW)
Q2206–199N	2.559	17.49	Savage <i>et al.</i> (1978) Sargent <i>et al.</i> (1988) Pettini <i>et al.</i> (1990) (PHSM) Rauch <i>et al.</i> (1993)
Q2348–147	2.940	16.9	Pettini <i>et al.</i> (1994) Monk <i>et al.</i> (1995)

The IPCS detector consists of a photocathode backed by an image intensifier tube. It was adjusted to produce rectangular pixels $19\ \mu\text{m}$ wide in the echelle dispersion direction and $77\ \mu\text{m}$ wide in the cross-dispersion direction. The IPCS provides 2048×256 pixels (echelle dispersion \times cross-dispersion), but a software window consisting of the central 2040×240 pixels was used to avoid spurious signals at the detector edges. This resulted in a detector format $38.8 \times 18.5\ \text{mm}$, which is shown on the echellogram in Figure 4.1. As can be seen from the echellogram, the size of the IPCS window does not allow full coverage of the orders for wavelengths $\gtrsim 3300\ \text{\AA}$. Since all observations for this thesis were made at $\lambda > 3300\ \text{\AA}$, there are small gaps in the wavelength coverage between each of the echelle orders.

Charge-coupled device (CCD) detectors are also available for use with UCLES. The IPCS was chosen for a combination of reasons. It has a very low dark count rate, 5–20 times lower than the CCDs, and is unaffected by readout noise or cosmic ray strikes. The combination of these effects renders the available CCDs effectively useless for observing faint QSOs with UCLES, since the combined noise would swamp the signal. Two incidental advantages of the IPCS over the CCDs are the larger detector, allowing greater wavelength coverage, and the smaller pixel size, allowing higher resolution.

The spectrograph entrance slit was set to a projected width of 1.0 arcsec on the sky, corresponding to 2.8 IPCS pixels in the echelle dispersion direction. The spatial separation between adjacent orders was sufficient to allow a projected slit length of ~ 20 arcsec without overlap between the orders, corresponding to ~ 20 pixels in the cross-dispersion direction. (One pixel in the cross-dispersion direction projected to 0.9 arcsec on the sky. The exact slit length varied with different wavelength coverages.) The length of the slit allowed adequate recording of the adjacent sky background for later subtraction.

Table 4.2 Details of QSO echelle observations.

Object	Date	λ Range (\AA)	Echelle Orders	Exposure (s)
1101–264	1989 Mar 11	3390–3848	66–59	4 890
	1989 Mar 12			21 330
	1990 Feb 04			17 150
	1990 Feb 19			8 360
	1990 Feb 21			6 440
	1990 Feb 23			6 000
	1990 Feb 24			22 950
	1991 Feb 19			22 320
	1991 Feb 20			16 310
	1991 Feb 21			3 300
Total		3390–3848	66–59	129 050
2348–147	1991 Aug 10	4002–4842	56–47	14 510
	1991 Aug 11			23 700
	1991 Aug 12			6 000
	1991 Aug 13			6 000
	1992 Aug 26	3921–4743	57–48	15 000
	1992 Aug 27			18 000
	1992 Aug 28			12 269
	1993 Aug 19	3728–4382	60–52	15 000
	1993 Aug 20			21 600
	1993 Aug 21			23 400
	1993 Aug 22			21 000
	Total			4768–4842
		4392–4743	51–48	95 479
	4002–4382	56–52	176 479	
	3921–3988	57	126 269	
	3728–3919	60–58	81 000	

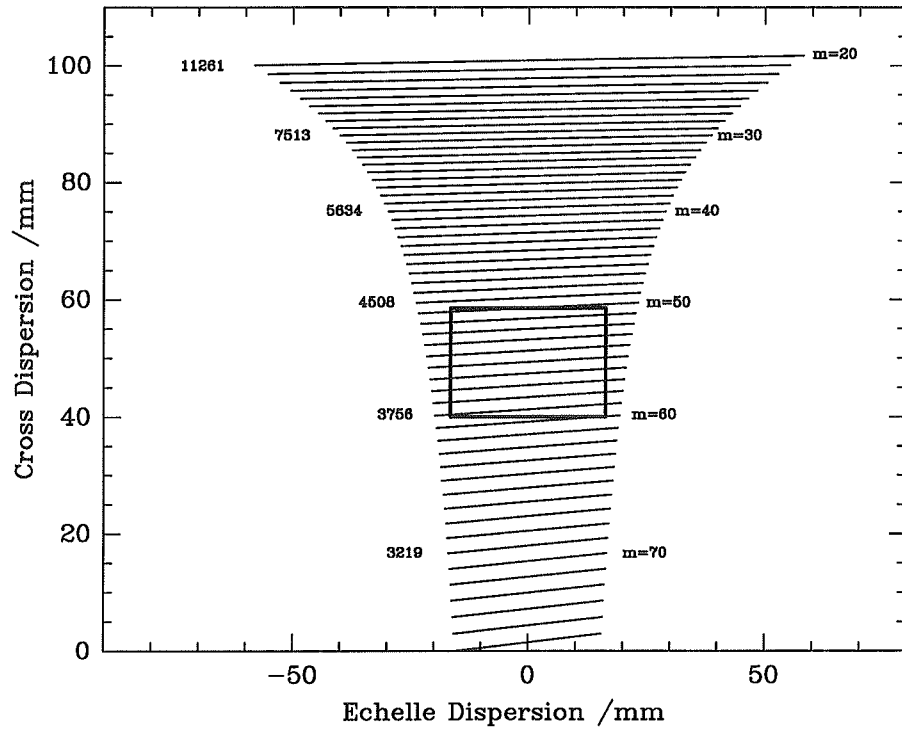


Figure 4.1 UCLES echellogram for the 79 grooves mm^{-1} echelle grating. The positions of the spectral orders in the detector plane are shown as tilted lines. The rectangular box shows the size of the IPCS detector window. In practice, the camera head is rotated slightly so the orders are more closely parallel to the rows of pixels. The order numbers (m) are shown on the right and the central wavelengths of the labelled orders, in Angstroms, are shown on the left.

In this configuration, UCLES and the IPCS provide a resolving power $\lambda/\Delta\lambda = 43\,000$, corresponding to a spectral resolution of 7.0 km s^{-1} .

Observing Details

The echelle observations of each QSO were made with separate integrations of 3000 seconds each, interrupted when necessary because of cloud cover or the approach of astronomical twilight. The seeing was generally between 1 and 2 arcsec, with occasional brief fluctuations > 2 arcsec. Data collection was stopped on the few occasions when the seeing stayed > 2 arcsec for extended periods and a backup program (unrelated to the work in this thesis) was pursued. All the data were acquired during dark of moon.

The projection of the spectrograph slit on the sky was kept at the parallactic angle throughout the observations by the use of a beam rotator. This was to ensure the atmosphere dispersed the light only along the direction of the slit, avoiding any

wavelength-dependent vignetting by the slit.

Each QSO was positioned at a point one-third of the way along the slit, to allow several contiguous pixels to record the sky background. Every few exposures, the position of the QSO was moved to a point one-third of the way from the opposite end of the slit, to reduce the effect of any pixel-to-pixel variations in the detector sensitivity. Approximately half the exposures taken on each night were made at each position.

Calibration spectra of a standard thorium-argon comparison lamp were taken at the beginning of each night's observing, after every two exposures, and at the end of the night's observing. A spectrum of a B star was also taken each night, for purposes of tracing the echelle orders. The IPCS has inherent non-linearities in its frame format, so the spectral orders from UCLES appear distorted in an S-shape rather than in a straight line parallel to the rows of pixels. This can be seen in a raw data frame, shown in Figure 4.2.

A flat field spectrum of an incandescent quartz lamp was taken at least once during each observing run (9999 s exposure, taken during the day). This was used only to check that the IPCS response was smooth on large scales. No flat field corrections of pixel-to-pixel sensitivity variations are required for the IPCS at the count levels of the present observations.

4.2.2 Reduction of Raw Data

Reduction of the raw echelle data was performed with the FIGARO software package (Shortridge, 1990), following the procedure outlined by Robinson *et al.* (1989).

Removal of S-Distortion

The S-distortions of the echelle spectral orders for each night were traced with the corresponding B star spectrum and fitted with fifth order polynomials by the routine SDIST. These fits were used to straighten the frames of QSO and comparison arc spectra, using the CDIST routine.

Summation of Nightly Data

Rows of the comparison lamp spectra taken during each night were extracted and cross-correlated between exposures to check the amount of wavelength drift during each night. In every case, the drift was negligible, being < 0.1 pixels. QSO frames at each slit position and comparison frames from each night were added together. Data from different nights were kept completely separate at this stage.

Extraction of Nightly Spectra

The echelle orders were extracted from the two dimensional IPCS frames using the ECHSELECT routine. Generally the three rows of pixels (corresponding to ~ 2.7 arcsec on the sky) with the highest number of photon counts (integrated

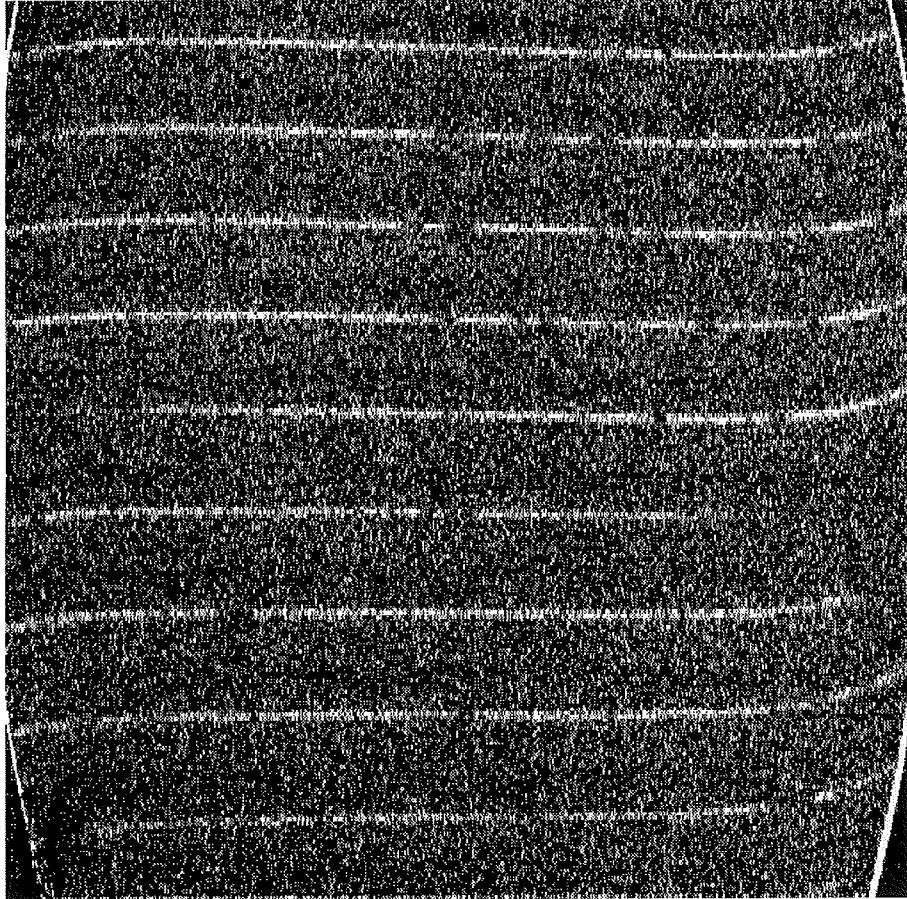


Figure 4.2 Raw IPCS frame for Q2348–147. Nine spectral orders are visible—orders 60–52. The wavelength increases from left to right along each order, and from bottom to top across the orders. The bright lines are the spectrum of the QSO. Several absorption features can be seen as gaps in the bright lines, including the $z_{\text{abs}} = 2.279$ damped Lyman α line at the right end of order 57 (sixth from the top). Most of the remainder of the frame is the sky background, except for the narrow gaps between the spectral orders, which may be discerned as dark lines two-thirds of the distance down from one bright line to the next. The S-distortion of the spectral orders can be seen clearly. The bright arcs in the corners are artefacts at the edge of the IPCS tube.

along the rows) were summed to form the object spectrum, and nine rows of pixels were summed to form the sky spectrum. In terms of Equation 1.10, $n_{\text{obj}} = 3$ and $n_{\text{sky}} = 9$. Occasionally, when the QSO profile along the slit direction was centred close to a pixel boundary, the four highest rows of pixels were used for the object spectrum ($n_{\text{obj}} = 4$). The spectra extracted by ECHSELECT were automatically normalised to maintain the correct relative intensities. The resulting sky spectra were subtracted from the object spectra.

Comparison spectra were extracted for each night from the summed arc lamp frames, for both QSO slit positions, using the same pixel rows as the extractions of the corresponding object spectra.

Optimal extraction of the object spectra (Robertson, 1986) was not performed because a software facility for doing so was not available during most of the data reduction.

Wavelength Calibration

Wavelengths of emission lines in the comparison arc spectra were identified using the Anglo-Australian Observatory thorium-argon arc line atlas (Bessell and Pettini, 1991). A wavelength scale was fitted to each echelle order of the summed comparison spectra for each night and each QSO slit position with a fifth order polynomial using the routine ECHARC. The RMS residuals were generally less than 0.007 \AA . The resulting wavelength values for each pixel were copied on to the sky-subtracted QSO spectra.

The velocity corrections appropriate to convert each night's spectra to the heliocentric frame were calculated using the Starlink program RV. The wavelength scales were adjusted to the heliocentric frame using the calculated corrections, and to vacuum, using the routine VACHEL.

The resolutions of the spectra were measured by calculating an average full-width-at-half-maximum for several strong arc lines in each comparison spectrum. The resolutions varied from $0.08\text{--}0.11 \text{ \AA}$, depending on wavelength—close to the values expected from the resolving power.

Scrunching and Summing of Data

The spectra from each QSO position on each day were rebinned on to a common wavelength grid (for each object), maintaining approximately the same wavelength sampling as the raw data. This was done with the quadratic interpolation function of the routine SCRUNCH. Then all of the data for each object were added together, giving a sky-subtracted, unnormalised spectrum.

A complication occurred at this stage with the data for Q2348–147. The data collected in August 1993 shared five orders in common with older data for the same object, but the placement of the IPCS window on the echellogram was shifted considerably in the echelle dispersion direction. The result was that extra spectral regions in the inter-order gaps of the earlier data were covered, while a similar

wavelength range was missed at the opposite end of each of the orders which had been covered previously.

The small sections of spectrum which were covered only by the August 1993 observations were reduced separately because the count levels were much lower than those in the adjacent, fully covered, orders. Nevertheless, they provide useful data on some absorption lines not covered by the rest of the spectrum. These small sections were named orders 56a to 52a, since they adjoin orders 56 to 52 respectively. They are shown plotted (normalised) in Figure A.5, together with the rest of the Q2348–147 spectrum.

4.2.3 Continuum Fitting and Profile Fitting

The continuum and profile fitting procedures for the high resolution QSO data generally followed the same processes used for the Cloudy Night QSO, described in Section 2.2.

Continua were fitted to the spectral orders of each object using the program DIPSO (Howarth *et al.*, 1993). Continuum points were judged by eye in regions apparently free of absorption and fitted with cubic splines using the CFIT command. An effort was made to keep the continua smooth, consistent with the known UCLES/IPCS sensitivity profile and QSO emission lines. The continuum fits were scrutinised by Max Pettini, who suggested minor changes to some spectral orders. When the fits were finalised, the data were normalised by dividing by the fitted continua.

In principle a flux standard could have been used to provide response curves for each echelle order, which would assist the continuum fitting process. However, this is not practicable for spectra of such high resolution, since current spectrophotometric standards are not sampled at high enough resolution. Typical standards may only provide a handful of points across a whole echelle order—inadequate for deriving any useful response curve.

The spectra were examined visually for likely absorption lines. Wavelengths and equivalent widths of these lines were measured using the EW command in DIPSO. This command also gives an uncertainty estimate σ in the equivalent widths, based on the unnormalised count level in the continuum near each line. Lines with equivalent widths above 6σ were compiled into lists for each QSO. Apparent lines near or slightly below the 6σ limit were also measured to ensure no lines above the chosen cut-off were missed.

The normalised spectral orders for Q1101–264 are shown in Figure A.4 and the normalised spectral orders for Q2348–147 are shown in Figure A.5, both in Appendix A. The Figures show the positions of the detected absorption lines, marked with vertical lines.

The absorption line profiles were fitted interactively using the program Xvoigt (Mar and Bailey, 1995, see also Appendix C). The procedure followed was identical to that used on the CNQ data, described in detail in Section 2.2.

Table 4.3 Details of intermediate spectral resolution CCD observations of Q2348–147.

Object	Detector	Date	λ Range (\AA)	Exp ¹ (s)	RMS arc fit Residuals (\AA)	Resolution (\AA)
2348–147	Blue Thomson	1991 Dec 09	4801–6075	3000	0.04	2.9
	Blue Thomson	1992 Jun 04	4801–6075	1800	0.03	2.9
	Tek 1k	1992 Sep 30	6808–8420	4000	0.10	2.9

Notes:

¹ Exposure time.

The line fit parameters for Q1101–264 are shown in Table B.6 and the line fit parameters for Q2348–147 are shown in Table B.8, both in Appendix B. The line numbers in the Tables correspond to those marked on the spectra in Figure A.4 and Figure A.5.

4.3 Intermediate Resolution Observations of Q2348–147

To complement the UCLES spectra of the Lyman α forest region of Q2348–147, intermediate resolution spectra of the region redward of the Lyman α emission peak were also obtained at the AAT. The spectra were obtained to facilitate the search for heavy element absorption systems along the sightline to the QSO.

These were service observations made with the Royal Greenwich Observatory Spectrograph (Robinson, 1985) and CCD detectors, all by Raylee Stathakis; details are given in Table 4.3. Calibration spectra of a standard copper-argon comparison lamp were taken before and after each exposure. Standard star and flat field exposures were also taken on each date.

Access was also available to a 1.4 \AA resolution observation of the wavelength range 6320–6950 \AA from Pettini *et al.* (1994). This spectrum contained no detectable absorption lines, so is not discussed further.

No intermediate resolution spectra of Q1101–264 were required, since adequate spectra redward of Lyman α emission have been published (Boissé and Bergeron, 1985; Petitjean and Bergeron, 1990).

4.3.1 Description of Data Reduction

Initial reduction of the CCD data was performed with the FIGARO software package (Shortridge, 1990). A bias value for each frame was determined by averaging the counts over a bias area of the frame, excluding pixels near the edges of the bias area. The appropriate bias value was then subtracted from each object frame. Cosmic ray strikes were cleaned manually from the object, standard star, and comparison lamp frames using the routine CLEAN.

The object frames were collapsed in the y-direction to determine in which rows the object appeared. Three or four rows of pixels were chosen and the object spectra were extracted from these rows using the EXTRACT routine. Sky spectra were extracted in two different ways:

- For spectra taken before 1992, September 30, the sky was extracted from several rows of pixels adjacent to the object rows.
- For the spectrum taken on 1992, September 30, the sky spectrum was formed using the routine POLYSKY, which interpolates the level of the sky in the same rows as the object by fitting a polynomial to the count level around it.

The resulting sky spectra were subtracted from the object spectra.

Calibration lamp spectra were extracted from the same frame rows as the object spectra. Comparison emission lines were identified with the Anglo-Australian Observatory copper-argon arc line atlas (Stathakis *et al.*, 1986). A wavelength scale was fitted to each calibration spectrum with a fifth order polynomial using the routine ARC. The resolution was measured by taking the average FWHM of the identified comparison lines. The RMS residuals to the arc fit and the resolution are shown in Table 4.3. The resulting wavelength scale was copied onto the sky-subtracted QSO spectra.

The wavelength scale was adjusted to the vacuum-heliocentric frame using the routine VACHEL and the heliocentric velocity correction calculated using the Starlink program RV. The spectra were then mapped to 1.2 Å bins using the quadratic interpolation routine SCRUNCH. The two spectra taken with the Blue Thomson CCD detector were added to produce a total spectrum.

The wavelengths of apparent absorption lines were measured using the EW command in DIPSO and an attempt was made to identify the lines, in conjunction with the echelle data. Absorption lines in the CCD spectra, being redward of the Lyman α emission peak, are caused by metal absorption in intervening heavy element systems. These data were therefore valuable for identifying such systems and minimising metal contamination of the Lyman α line samples gathered from the UCLES data.

The reduced CCD spectra of Q2348–147 are shown in Figure A.6 in Appendix A. The identified metal lines in these spectra are listed in Table B.10 in Appendix B, and their positions are indicated by vertical lines in Figure A.6.

Chapter 5

Heavy Element Absorption Systems

5.1 Introduction

In order to study the properties of the Lyman α absorption lines along the lines of sight to QSOs, one must first attempt to identify which lines are produced by which elements. If the available data do not allow the identification of Lyman α lines by matching redshifts with other Lyman series lines, then as many heavy element lines as possible must first be identified. After this process of elimination, the remaining unidentified lines are then assumed to be caused by Lyman α absorption.

There is likely to be some level of misidentification in the process of assigning lines to specific elements. This is discussed in detail in Section 3.6.

Heavy element systems form an interesting subject of study in themselves. Some of the data presented in this thesis have formed part of a study by Pettini *et al.* (1995) on metal abundances in the early universe.

This Chapter gives details of all of the heavy element absorption systems detected in the spectra of the QSOs 1101–264 and 2348–147. These systems are not studied further in this thesis.

5.2 Searching for Heavy Element Systems

The method of searching for heavy element systems in the spectra of Q1101–264 and Q2348–147 was identical to that used on the Cloudy Night QSO data, described briefly in Section 2.2.

In detail, the procedure involved was as follows:

- Many of the lines in the intermediate resolution spectra redward of Lyman α emission could be readily identified (being easily recognised doublets, for example). This established some redshift systems immediately. In the case of Q1101–264, several redshift systems were known from published data.

- A preliminary visual inspection was made of the echelle data for obvious metal lines such as doublets and likely associated lines at the same redshift as established systems.
- The vacuum wavelengths of the remaining unidentified lines (in both the echelle and intermediate resolution spectra) were entered into a computer program which searched for redshift coincidences between all possible pairs of lines. Since this has the potential of producing vast numbers of coincidences, a heuristic ranking of possible systems was applied. Possible systems with larger numbers of lines were ranked more highly than ones with fewer lines, and lines which were more closely coincident in redshift were ranked higher than lines with large redshift discrepancies.
- The most highly ranked possible systems identified by the computer program (about 100 for each object) were all examined manually to determine the reality of each system. This was done by comparing the redshift matches, line profiles, and relative strengths of the lines. Often systems could be rejected based on poor matches between detailed structure of the lines or the relative strengths being inconsistent with that expected from ratios of oscillator strengths.
- When a redshift system was established, lines from several other metal transitions were searched for at the same redshift. Also, since heavy element systems tend to cluster in redshift space, lines near the identified lines were checked to see if they defined another system at a similar redshift.
- Since metal lines generally have $b < 10 \text{ km s}^{-1}$, all unidentified narrow lines were manually cross-checked with each other to find any possible matches for metals at a common redshift that may have been ranked too low by the computer program to have been considered earlier. These lines were also checked to see if they could be identified in any of the established redshift systems.
- The metal line wavelengths in the search list were multiplied by $(1 + z_{\text{abs}})$ for each of the established systems to search for any metal lines in these systems that may have been blended with other lines, or that may be present at just under the 6σ confidence limit used to define the line samples.
- Keith Lipman assisted by attempting to find any further metal identifications. He used a spreadsheet to calculate wavelength ratios, looking for matches to known transitions, and examined the spectra manually.
- The identifications were tabulated and discussed with Richard Hunstead. Several tentative identifications were either accepted or rejected based on close scrutiny of the line profiles and the implied physical conditions of the absorbing gas.

A list of the metal lines used in these searches, taken from Morton *et al.* (1988), is given in Table B.1 in Appendix B.

5.3 Heavy Element Systems in Q1101–264

This Section describes each of the metal line systems identified in the Q1101–264 spectrum. Most of these systems have also been identified and described by Carswell *et al.* (1982), Carswell *et al.* (1984), Boissé and Bergeron (1985), Petitjean and Bergeron (1990), and Carswell *et al.* (1991, hereafter CLPW). The absorption lines are referred to by the line numbers shown in the first columns of Tables B.6 and B.7 in Appendix B, and are marked on Figure A.4 in Appendix A. Occasionally line numbers from CLPW are referred to; this is mentioned explicitly in each case.

5.3.1 Definite Redshift Systems

$$z_{\text{abs}} = 0.359$$

This is an established system first found by Carswell *et al.* (1984), who identified two components in Mg II $\lambda\lambda 2796, 2803$ and a single component of Fe II $\lambda 2600$. With higher resolution observations, CLPW fitted seven components to the Mg II complex and found an additional Fe II component corresponding to the second strongest Mg II feature.

With the higher S/N data used here, only five components are found to be necessary to fit the Mg II complex (lines 138–142, 147–151). The fits to the complex are shown in Figure 5.1. The two components of CLPW at $z_{\text{abs}} = 0.358950, 0.358972$, which together form the deepest absorption feature, are fitted here with a single line at $z_{\text{abs}} = 0.358965$. This is a good fit to both lines of the doublet and there is no evidence for the existence of the two sub-components found by CLPW. It is interesting to note that CLPW do not claim the sub-component structure for the strongest Fe II $\lambda 2600$ feature, preferring to fit a single line. Based on the evidence available, I conclude there is only a single component at $z_{\text{abs}} = 0.358965$ and that CLPW's sub-components are not real. The seventh line of CLPW's fit is seen as an additional weak line to the red of the $\lambda 2796$ complex (line 143). It is not seen in the $\lambda 2803$ line, possibly because of S/N effects, and is therefore only tentatively identified here as a Mg II component. The other Mg II components are in agreement with those of CLPW.

The two Fe II $\lambda 2600$ components seen by CLPW are confirmed (lines 63, 64), and a third (line 65), corresponding to the third strongest Mg II component, is found.

$$z_{\text{abs}} = 1.187$$

This system was found by Boissé and Bergeron (1985) on the basis of a Mg II $\lambda\lambda 2796, 2803$ doublet. Petitjean and Bergeron (1990) found two Mg II components and one corresponding component of Fe II $\lambda 2600$. CLPW detected Al II $\lambda 1670$ in the same two components, at $z_{\text{abs}} = 1.186824, 1.187499$ (lines 40a, 41 from CLPW; see Figure 5.2). CLPW also fitted two broad ($b = 32.7 \pm 12.7, 71.7 \pm 29.1$) Lyman α features centred 0.14 \AA redward of their line 40a (line 40b from CLPW) and 1.06 \AA redward of their

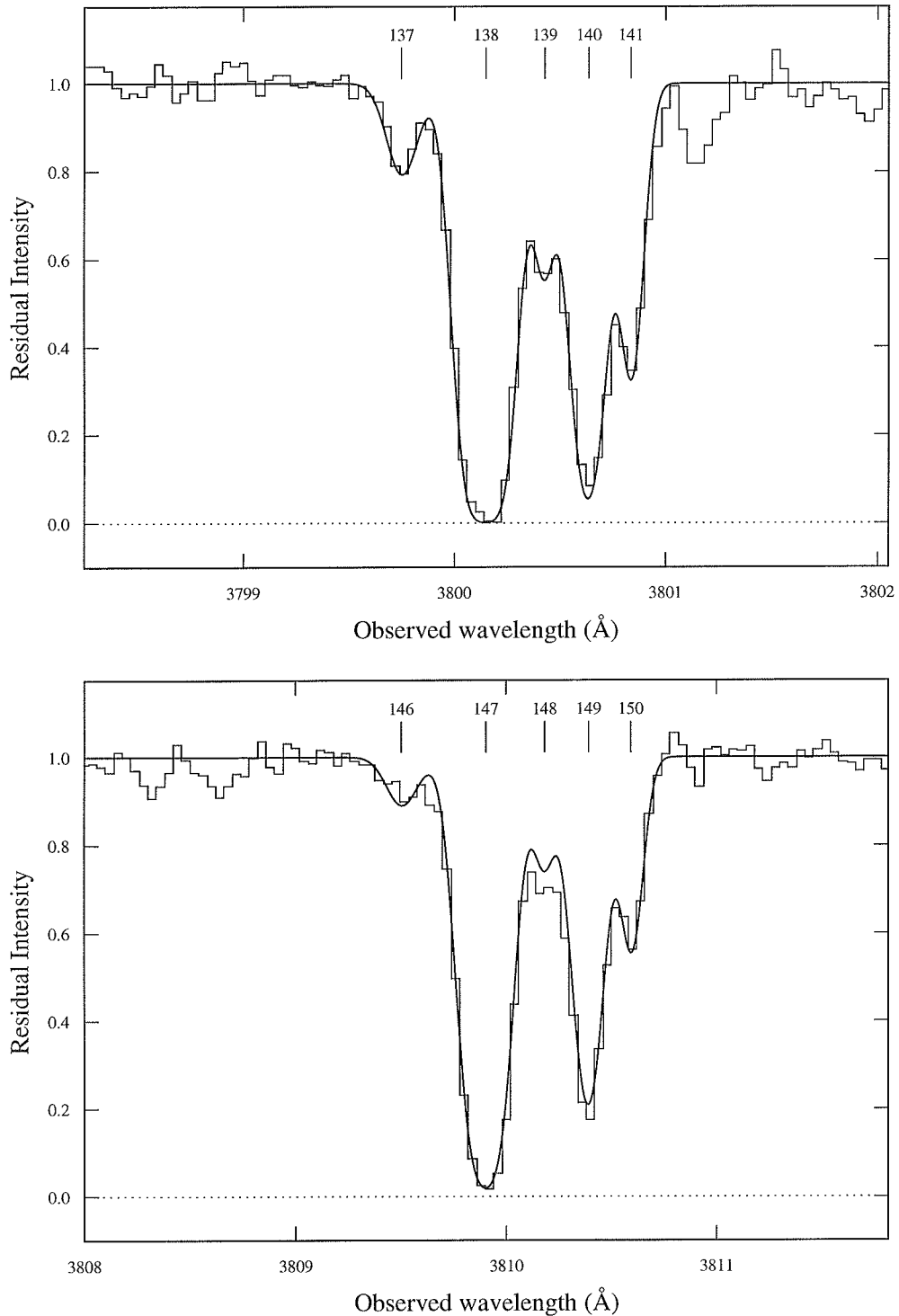


Figure 5.1 Profile fits to the $z_{\text{abs}} = 0.359$ Mg II complex in the Q1101–264 spectrum. All line numbers are from Table B.6. The fits to the doublet are simultaneous—using the same redshifts, velocity dispersions, and column densities for both transitions. *Top*: The Mg II $\lambda 2796$ line. *Bottom*: The Mg II $\lambda 2803$ line.

line 41 (line 42 from CLPW), respectively, but stated the continuum level near these lines was uncertain.

In the data studied here there is no evidence for the broad Lyman α lines fitted by CLPW. This can be seen in a comparison between CLPW's fits and my fits, shown in Figure 5.2. CLPW's line 40b is an overly broad fit to a feature identified here as an additional Al II $\lambda 1670$ component (line 89). CLPW's line 42 does not appear to be present—there is a slight depression of the continuum in the area, but not enough to form a significant line. CLPW's line 41 is seen to be composed of two blended Al II lines of similar strength (lines 90, 91).

There are absorption features at the expected wavelengths of C IV $\lambda 1550$ for each component, but at the bluemost edge of the spectrum where the S/N ratio is poor and the continuum level uncertain. A narrow feature (line 3) appears near the redshift of the redmost Al II component (line 91), but the match is not very good. A broad feature (line 2), which is probably blended with Lyman α , is centred at the redshift of the bluemost Al II component (line 88) and could easily conceal C IV components corresponding to all the other Al II lines. There is an additional narrow feature further to the blue (line 1), which is tentatively identified as an additional C IV $\lambda 1550$ line. The corresponding Al II $\lambda 1670$ line would be near the centre of the Lyman α feature at 3652.42 \AA (line 87), but there is no evidence of this component in Mg II in Petitjean and Bergeron's red spectrum. Therefore, if this possible identification is correct, it would correspond to a high ionisation component in which Mg II would be too weak to have been detected.

$$z_{\text{abs}} = 1.203$$

This system was also identified from a Mg II $\lambda\lambda 2796, 2803$ doublet by Boissé and Bergeron (1985). Petitjean and Bergeron (1990) reported three Mg II components, with the central one stronger than the two flanking components, which were of about equal strength. Somewhat surprisingly, CLPW found only the central and redmost component in Al II $\lambda 1670$.

The finding of CLPW that the bluemost Mg II component does not appear in Al II is confirmed here at the chosen 6σ line detection limit, but there does appear to be a weak absorption feature in our data centred at the expected wavelength. This is shown in Figure 5.3, which shows my fits to the Al II $\lambda 1670$ complex. This feature (marked with an "X" in the Figure) is almost certainly the Al II line, but its equivalent width is only \sim half that of the detected redmost line. Since these data are at much higher resolution than those of Petitjean and Bergeron, and the lines are unsaturated (*i.e.* on the linear part of the curve-of-growth), it is concluded that the cloud producing the redmost absorption (line 96) contains \sim twice as many absorbing atoms as the one producing the bluemost absorption (line X).

The similar strengths of the Mg II components in Petitjean and Bergeron's data are most likely because the lines are partially saturated and unresolved. The equivalent width ratio of the doublet for the redmost component is $W_{2796}/W_{2803} = 1.0$ while for the bluemost it is $W_{2796}/W_{2803} = 1.5$. This indicates the redmost compo-

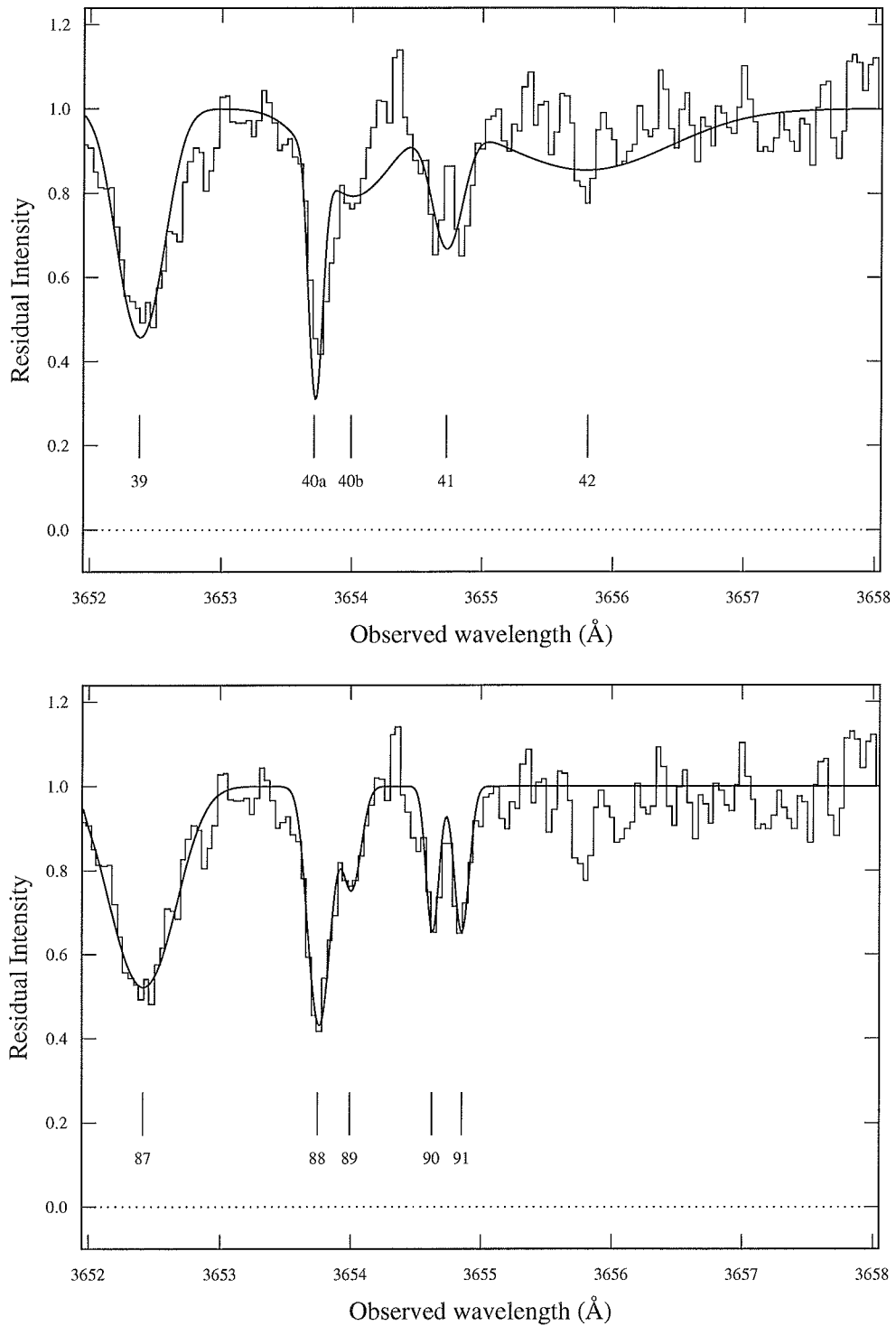


Figure 5.2 Profile fits to Al II $\lambda 1670$ in the $z_{\text{abs}} = 1.187$ system of the Q1101–264 spectrum. *Top:* CLPW’s fits superimposed on our data. The line numbers are from CLPW. Lines 40a and 41 were claimed as Al II $\lambda 1670$; the others were attributed to Lyman α . *Bottom:* My fits, with line numbers from Table B.6. Lines 88–91 are all identified as Al II.

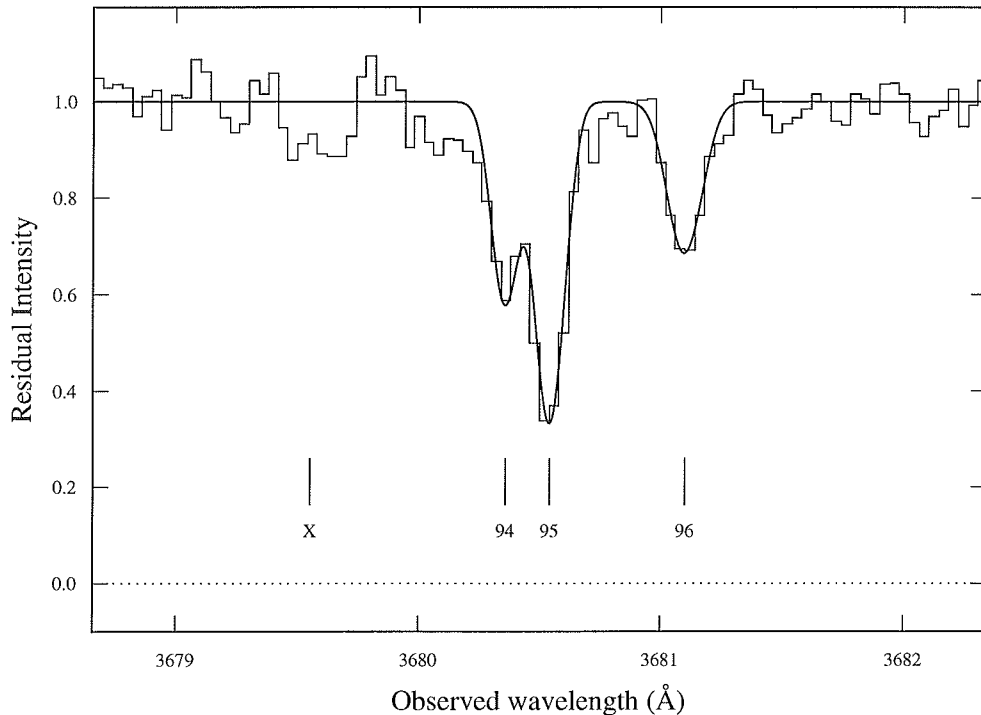


Figure 5.3 Profile fits to the Al II $\lambda 1670$ complex in the $z_{\text{abs}} = 1.203$ system in the Q1101–264 spectrum. My fits are shown, with line numbers from Table B.6. The expected position of Al II $\lambda 1670$ at the redshift of Petitjean and Bergeron (1990)’s bluemost Mg II component is marked with an “X”.

ment is fully saturated, while the bluemost is partially saturated¹. The similarity of strength in Mg II can then occur if the redmost component has a velocity dispersion less than that of the bluemost. A Voigt profile fit to the weak ($< 6\sigma$) Al II feature (X) gives $b = 10 \pm 3 \text{ km s}^{-1}$, which is consistent with being greater than the $b = 7 \pm 2 \text{ km s}^{-1}$ of the redmost Al II line, so this explanation is consistent with all the available data. The Mg II doublet ratio for the redmost component can also be calculated by assuming the relative Mg/Al abundance in the absorbing cloud is similar to solar ($[\text{Mg}/\text{Al}] = 1.11$ from Anders and Grevesse, 1989) and using the measured Al II column density to estimate that for Mg II. When this is done, also assuming the velocity dispersions of both species are the same, the estimated doublet ratio is $W_{2796}/W_{2803} = 1.6$, which is inconsistent with the 1.0 of Petitjean and Bergeron. This may indicate that the redmost component consists of two or more narrower, blended components, since lower b values will produce a Mg II doublet ratio closer to unity.

CLPW’s central component of Al II (CLPW’s line 45) is seen in our data to consist of two blended, narrow components (lines 94, 95). The C IV $\lambda\lambda 1548, 1550$ doublet is also seen in this system for the first time. It reveals a much more com-

¹The ratio is $W_{2796}/W_{2803} = 2.0$ for lines on the linear part of the curve-of-growth.

plex velocity structure than Al II, requiring a minimum of ten components to give satisfactory fits to both the $\lambda 1548$ (lines 6–15) and $\lambda 1550$ (lines 16–25) lines.

$$z_{\text{abs}} = 1.267$$

This system was identified by Petitjean and Bergeron (1990) on the basis of a weak Mg II $\lambda\lambda 2796, 2803$ doublet. The only additional line detected here is C IV $\lambda 1548$ ². There is a strong line matching Petitjean and Bergeron's redshift (line 52), and a weaker, narrow line 0.59 \AA (50 km s^{-1}) to the blue (line 51) which is also tentatively identified as C IV $\lambda 1548$. The corresponding C IV $\lambda 1550$ lines are within the saturated Lyman α feature at 3515.92 \AA (line 54). Al II $\lambda 1670$ lies in an inter-order gap, but CLPW note it is undetectable because it falls within the C II $\lambda 1334$ complex of the $z_{\text{abs}} = 1.838$ system. The lack of any detectable Fe II $\lambda 1608$ noted by CLPW is confirmed.

$$z_{\text{abs}} = 1.477$$

This system was discovered by Carswell *et al.* (1982) on the basis of the C IV $\lambda\lambda 1548, 1550$ doublet. CLPW fitted three components to the doublet, and found a broad feature partially covering the expected position of the strongest Si IV $\lambda 1402$ component. They fitted the strongest Si IV line possible using the same velocity dispersion as the corresponding C IV component and attributed the rest of the equivalent width to a blended Lyman α line. The Si IV $\lambda 1393$ line falls in the saturated core of the damped Lyman α feature at $z_{\text{abs}} = 1.838$ (line 36), so it cannot be used to provide a more certain fit.

The data studied here confirm the three C IV components found by CLPW (lines 154–156, 158–160). There is an additional weak feature redward of the $\lambda 1548$ complex which is tentatively identified as C IV (line 157). Any corresponding $\lambda 1550$ component may not be detectable because of noise. The Si IV $\lambda 1402$ line is seen to contain the two strongest components (lines 43, 44), well-matched in redshift, with little or no evidence for the blended Lyman α component claimed by CLPW. The noise level at the Si IV line in CLPW's spectrum is high, which could account for the unusual shape of the feature in their spectrum.

$$z_{\text{abs}} = 1.838$$

This is a complex system first reported by Carswell *et al.* (1982), who found single, unresolved lines of Si II $\lambda\lambda 1190, 1193, 1260, 1304, 1526$, Si III $\lambda 1206$, Si IV $\lambda\lambda 1393, 1402$, O I $\lambda 1302$, C IV $\lambda\lambda 1548, 1550$, Al II $\lambda 1670$, and a damped Lyman α line in their low-resolution ($\sim 2 \text{ \AA}$ FWHM) spectrum. Carswell *et al.* found five components in the system, in Si II $\lambda\lambda 1260, 1526$, O I $\lambda 1302$, C II $\lambda 1334$, and C IV $\lambda\lambda 1548, 1550$. CLPW fitted seven components to the Si II $\lambda 1260$, O I $\lambda 1302$, and C I $\lambda 1334$ lines.

²This line was present in CLPW's spectrum, but they did not recognise it as a C IV line, instead attributing it to Lyman α .

A single Si II $\lambda 1304$ line was also identified by CLPW, nestled between two strong Lyman α features.

In the data here, only six components were fitted to Si II $\lambda 1260$ (lines 73–78), two of the closely blended components of CLPW being fitted by a single line. The O I $\lambda 1302$ complex required only four components (lines 99–102). There is a weak feature at the expected wavelength of O I for another component, but it falls below the 6σ line detection limit. Additionally, a feature blended with the red side of the O I complex is tentatively identified as O I (line 103), although there is no corresponding Si II $\lambda 1260$ feature. The single Si II $\lambda 1304$ line identified by CLPW is also seen (line 106).

Since the wavelength coverage here extends further to the blue than that of CLPW, the Si III $\lambda 1206$ line is also seen. This is a complex of several saturated and some unsaturated lines. Six components are required for an acceptable fit (lines 27–32), but five are saturated and blended so the component redshifts are somewhat uncertain and do not agree exactly with the Si II $\lambda 1260$ components. There may also be further structure present, but if so it cannot be discerned from the available data. An additional narrow line (line 33) just redward of the Si III complex is also tentatively identified as Si III. The corresponding Si II $\lambda 1260$ line would fall in the centre of a Lyman α feature (line 79), so may be present but undetectable.

The damped Lyman α line in this system is also seen (line 36), but is adjacent to an order edge, making the continuum level difficult to determine. However, the breadth of the damping wings still provides a strong constraint on the H I column density. The value measured is $\log N(\text{H I}) = 19.40 \pm 0.05$. The best fit value is identical to that measured by CLPW.

A weak, narrow line (line 5) is seen at the wavelength of N I $\lambda 1199$, corresponding to one of the strongest Si III $\lambda 1206$ components and the second strongest O I $\lambda 1302$ component. Since N I and O I co-exist at similar ionisation fractions due to charge exchange reactions with hydrogen (Spitzer, 1978), one would expect N I to be detectable at the redshift of the strongest component of O I. However, no corresponding N I $\lambda 1200.2$ line is seen, indicating either that the line is not N I $\lambda 1199$, or that the $\lambda 1200.2$ line is lost in the noise, which seems unlikely. Nevertheless, it is interesting to calculate the [N/H] abundance ratio assuming the line is indeed N I $\lambda 1199$. In this case, the abundance would be $[\text{N}/\text{H}] = -2.17 \pm 0.10$, which is an order of magnitude greater than the upper limit placed by Pettini *et al.* (1995) on the damped Lyman α system at $z_{\text{abs}} = 2.279$ in the spectrum of Q2348–147. This inconsistency, together with the other problems mentioned above, makes it highly unlikely that the line is N I $\lambda 1199$.

5.3.2 Possible Redshift Systems

$$z_{\text{abs}} = 0.238$$

This is a possible system not noted previously. The broad ($b = 33.0 \pm 9.5 \text{ km s}^{-1}$) line seen by CLPW at a wavelength of 3470.92 \AA is seen to be composed of two

narrow components (lines 40, 41), with fitted b values of 5 ± 2 and $6 \pm 2 \text{ km s}^{-1}$. A plausible identification for these lines is Mg II $\lambda 2803$ at $z_{\text{abs}} = 0.23798, 0.23804$. The expected positions of the accompanying $\lambda 2796$ doublet members fall close to the centres of Si II $\lambda 1526$ lines in the $z_{\text{abs}} = 1.267$ system (lines 37, 38). It is possible that the Mg II $\lambda 2796$ lines are blended with the Si II features. Unfortunately, there are no other identifiable lines in this possible system and there are no independent constraints on the strengths of the Si II lines which could reveal either the presence or absence of excess equivalent width caused by Mg II $\lambda 2796$. The existence of this system is therefore considered uncertain.

$$z_{\text{abs}} = 0.319$$

This is another possible new system, based on two weak, narrow lines seen at $\lambda = 3689.13$ and 3689.48 \AA (lines 97, 98). These lines have fitted b values of 6 ± 2 and $7 \pm 2 \text{ km s}^{-1}$, respectively, and have not been noted in any published work. If the lines are identified with Mg II $\lambda 2796$ at $z_{\text{abs}} = 1.31927, 1.31939$, then the corresponding $\lambda 2803$ doublet members are not seen, but they would be very weak—near or below the line detection threshold—and are in a noisy spectral region where the continuum may be ill-defined because of nearby strong lines (3698–3699 \AA , see Figure A.4). Fe II $\lambda 2600$ lines would be blended in the Lyman α line at 3429.93 (line 35) and in the noisy region just to redward of it. Lines as strong as lines 97 and 98 could be present without being detectable. No other reasonably strong lines would be expected to be seen within the spectral coverage of the data.

An alternative possibility for the identification of these lines exists. If the lines are identified as Si II $\lambda 1526$ at $z_{\text{abs}} = 1.41640, 1.41663$, then the expected positions of the C IV $\lambda\lambda 1548, 1550$ doublet fall in the strong Lyman α lines at 3740.88 and 3747.34 \AA (lines 115, 119). The $\lambda 1550$ component would be in the saturated core of line 119, but the $\lambda 1548$ component would be in the red wing of the strong line (115). The wings of line 115 are asymmetrical and consistent with a C IV column density of $N(\text{C IV}) \lesssim 1 \times 10^{13} \text{ cm}^{-2}$ at this redshift. The Si IV $\lambda\lambda 1393, 1402$ doublet would fall just to the blue of the wavelength coverage and all the other strong Si II lines are even further to the blue. (The Si IV doublet may be undetectable in any case, in a system with such low C IV column density.) The Al II $\lambda 1670$ line is to the red of the wavelength coverage. No published spectra cover any of these lines. The low resolution (8 \AA FWHM) red spectrum of Boissé and Bergeron (1985) does not show any sign of a Mg II $\lambda\lambda 2796, 2803$ doublet at this redshift. However, the Mg II lines in the strong $z_{\text{abs}} = 1.187$ and $z_{\text{abs}} = 1.203$ C IV systems appear quite weak in their spectrum, so if the ionisations are similar, a Mg II doublet in this proposed system could easily be below their detection limit. Since there is no conclusive evidence with which to verify or refute this system, it is also considered a possible identification.

Each of these alternative identifications and redshift systems must be considered tentative at best.

5.3.3 Spurious Redshift Systems

$$z_{\text{abs}} = 0.356$$

This is a system first proposed by Carswell *et al.* (1984) and subsequently claimed by CLPW on the basis of a Mg II $\lambda\lambda 2796, 2803$ doublet at 3792.68 and 3802.44 Å (lines 135, 144). CLPW noted the equivalent width ratio of the lines was nearly unity, so concluded the magnesium components must be nearly saturated. The fact that the features have a minimum residual intensity of ~ 0.5 was then used to infer a large number of blended narrow components. CLPW fitted a six-component decomposition of the features, using lines with velocity dispersions $b = 0.7, 0.8, 0.9, 1.4, 4.5,$ and 19.5 km s^{-1} . They also noted that no other lines were detected in this system, so the velocity structure could not be checked independently.

With the higher resolution and S/N ratio of my data, any component structure in these lines should be more easily visible. However, each of the features has a shape which is consistent with a single Voigt profile. The wavelengths are also not very well matched for a Mg II doublet complex. (My centroid wavelengths are slightly different to those of CLPW, being 3792.66 and 3802.47 Å, respectively.) These points are illustrated in Figure 5.4, which shows both lines overlaid in velocity space under the assumption that they form a Mg II doublet. Figure 5.4 also shows there is no obvious overall correlation of small-scale features between the two line profiles.

A simple calculation was done to estimate the probability that two lines in the Q1101–264 spectrum would have such a close match to a given doublet separation by chance. The centroids of the two lines are offset by 0.07 Å from the Mg II doublet wavelength ratio. The relevant probability then is that of a line falling within a specified “window” of four times³ this size: 0.28 Å. The spectrum covers 422 Å, so assuming a uniform random line distribution, the probability of a single line falling in such a window is $0.28/422 = 6.6 \times 10^{-4}$. Since 160 lines are detected in the Q1101–264 spectrum, the expected number of such a coincidences is given approximately⁴ by $160 \times 6.6 \times 10^{-4} = 0.11$. This is not an unreasonably low expectation, so the wavelength ratio coincidence should not be taken as strong evidence for the Mg II doublet identification.

Given the poor wavelength match, the fact that both lines are well-fitted by single Voigt profiles, the lack of any other identifiable lines at this redshift, and the fact that any possible Mg II component fits need to be contrived with several extremely narrow components to explain the doublet ratio, it is concluded that this is not a real metal line system and the absorption features are single Lyman α lines.

³Two times because the wavelength ordering of the random line pair is unimportant, and two times because the sense of the offset is unimportant.

⁴A full calculation of the expectation is complicated by the fact that some “windows” will fall outside the wavelength coverage or overlap each other, but the correction will be minor.

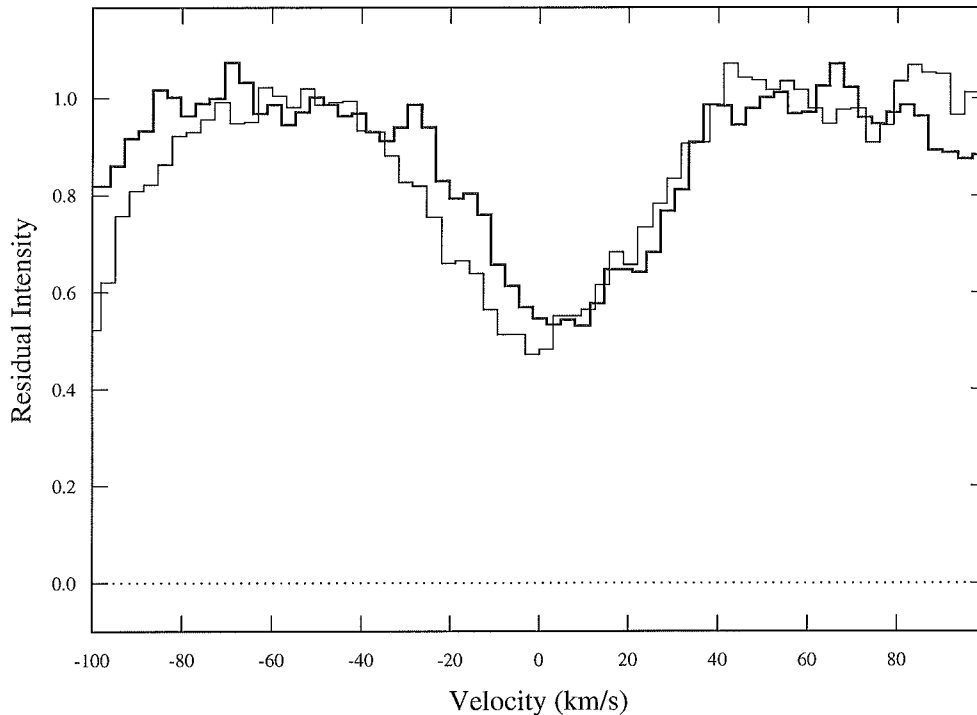


Figure 5.4 The lines reported by CLPW to be Mg II $\lambda\lambda 2796, 2803$ in the spectrum of Q1101–264, plotted on a velocity scale relative to $z_{\text{abs}} = 0.356288$ (assuming the identification is correct). The thin line shows the absorption feature at $\lambda = 3792.66 \text{ \AA}$ (line 135) and the thick line that at $\lambda = 3802.47 \text{ \AA}$ (line 144). The simple Voigt profile shapes of the lines and the velocity offset between them can be readily seen.

5.4 Heavy Element Systems in Q2348–147

This Section describes each of the metal line systems identified in the Q2348–147 spectrum. The absorption lines in the echelle spectra are referred to by the line numbers shown in the first columns of Tables B.8 and B.9 in Appendix B, and are marked on Figure A.5 in Appendix A. Absorption lines with wavelengths $\lambda > 5000 \text{ \AA}$ are from the intermediate resolution CCD spectra (see Section 4.3). These are listed in Table B.10 in Appendix B and shown in Figure A.6 in Appendix A. Lines from the CCD spectra have not been given line numbers.

$$z_{\text{abs}} = 1.819$$

This system contains a complex of three C IV $\lambda\lambda 1548, 1550$ doublets (lines 254–256, 257–259). The redmost component is saturated and may contain additional components, but it is difficult to tell from the available data.

Two lines of Si IV $\lambda 1393$ are also seen (lines 80, 81), corresponding to the strongest C IV components. These are in a noisy part of the spectrum. A possible feature at the redshift of the weakest C IV component is well below the 6σ line detection limit.

A C III $\lambda 1334$ line corresponding to the strongest component may be present, blended in the blue wing of the strong Lyman α line at 3763.61 \AA (line 14). Si II $\lambda 1526$ would fall in an inter-order gap, and other expected strong lines are outside the wavelength coverage.

$$z_{\text{abs}} = 1.923$$

This system is identified by a single C IV $\lambda\lambda 1548, 1550$ doublet (lines 303, 307), which is well matched in redshift ($z_{\text{abs}} = 1.92304$) and line strength. The doublet is partially saturated (doublet ratio $W_{1548}/W_{1550} \sim 1.6$). An Fe II $\lambda 1608$ line may also be present, blended with a broader Lyman α feature (line 361).

The expected position of O I $\lambda 1302$ is in the Lyman β line at 3806.01 \AA (line 32). There is no Si II $\lambda 1304$ feature and Si II $\lambda 1526$ would fall in the core of the strong Lyman α line at 4462.73 \AA (line 287).

$$z_{\text{abs}} = 2.279$$

This system contains a damped Lyman α line (line 105), which dominates much of order 57 of the echelle spectrum (see Figure A.5).

The best-defined component is at $z_{\text{abs}} = 2.27934$, and is detected in C II $\lambda 1334$ (line 264), O I $\lambda 1302$ (line 218), Si II $\lambda\lambda 1190, 1193, 1260, 1304$ (lines 71, 75, 166, 222, respectively), Si IV $\lambda 1402$ (line 325), and S II $\lambda 1259$ (line 164). The Si IV $\lambda 1393$ line is in an inter-order gap. Another component at $z_{\text{abs}} = 2.27830$ is detected in most of these lines (lines 70, 74, 165, 220–221, 262, 323) plus N V $\lambda\lambda 1238, 1242$ (lines 132, 137). There is also a line at the expected wavelength of Si III $\lambda 1206$ (line 95), but this and the N V lines are blended, probably with Lyman α lines. The $z_{\text{abs}} = 2.27934$ component cannot be identified convincingly in N V. There are several other components identified in two or more different lines—the noise and line blending make it difficult to determine if these components are real.

Several lines in this system are detected in the intermediate resolution CCD spectra: Si II $\lambda 1526$, C IV $\lambda\lambda 1548, 1550$, Al II $\lambda 1670$, and Fe II $\lambda\lambda 2344, 2374, 2382$.

The metal abundances in this system have been studied in detail by Pettini *et al.* (1995).

$$z_{\text{abs}} = 2.530$$

This system is detected only by a C IV $\lambda\lambda 1548, 1550$ doublet in the intermediate resolution CCD spectra and the saturated Lyman α line at 4290 \AA (line 226). There are no convincing identifications for Si II $\lambda\lambda 1190, 1193, 1260, 1304$, N I $\lambda\lambda 1199, 1200.2, 1200.7$, Si III $\lambda 1206$, O I $\lambda 1302$, or C II $\lambda 1334$ in this system. N V $\lambda\lambda 1238, 1242$ would fall in an inter-order gap, and other strong lines are outside the echelle wavelength coverage.

$$z_{\text{abs}} = 2.686$$

This system is detected only by a C IV $\lambda\lambda 1548, 1550$ doublet in the intermediate resolution CCD spectra and the saturated Lyman α line at 4480 \AA (line 480). Lines exist near the expected wavelengths of Si II $\lambda\lambda 1193, 1260$ (lines 267 and 347) and Si III $\lambda 1206$ (line 282), but the wavelength matches between the three lines are poor. There are no lines at the expected positions of N I $\lambda\lambda 1199, 1200.2, 1200.7$, O I $\lambda 1302$ or Si II $\lambda 1304$, and Si II $\lambda 1190$ and N V $\lambda\lambda 1238, 1242$ would fall in an inter-order gap.

$$z_{\text{abs}} = 2.727$$

This system is detected only by a C IV $\lambda\lambda 1548, 1550$ doublet in the intermediate resolution CCD spectra and the saturated Lyman α line at 4531 \AA (line 305). There is a strong line near the expected wavelength of Si II $\lambda 1260$ (line 360), but no corresponding lines of Si II $\lambda\lambda 1190, 1193, 1304$ are seen so this cannot be a correct identification. The position of N V $\lambda 1238$ is obscured by blended lines, but there is no line at the expected wavelength of N V $\lambda 1242$. Si III $\lambda 1206$ and O I $\lambda 1302$ are not detected either. N I $\lambda\lambda 1199, 1200.2, 1200.7$ would fall in an inter-order gap.

$$z_{\text{abs}} = 2.819$$

This system is detected by a C IV $\lambda\lambda 1548, 1550$ doublet and an Fe II $\lambda 2600$ line in the intermediate resolution CCD spectra and the saturated Lyman α line at 4643 \AA (line 346). There are no lines at the expected wavelengths of Si II $\lambda\lambda 1190, 1193, 1260$, N I $\lambda\lambda 1199, 1200.2, 1200.7$, Si III $\lambda 1206$, or N V $\lambda 1238$. Other strong lines are outside the echelle wavelength coverage.

5.4.1 Unidentified Lines

There remains one particularly puzzling group of unidentified absorption lines in the spectrum of Q2348–147. The lines between 4820 \AA and 4830 \AA (lines 380–383), which include two lines with $b < 10 \text{ km s}^{-1}$, could not be identified in any redshift system.

The lines can be ruled out as members of doublets such as C IV $\lambda\lambda 1548, 1550$ and Mg II $\lambda\lambda 2796, 2803$, and do not appear to correspond to any other reasonable identification. If they are Lyman α lines, they are at $z_{\text{abs}} \sim 2.969$, which is 0.029 greater than the nominal emission redshift of the QSO.

For the analyses in this thesis, these lines were assumed to be produced by Lyman α . It is, however, possible that some or all of them are metal lines for which any confirming lines in the same system are obscured or not within the redshift coverage of the spectra.

These lines are mentioned here because they are highly conspicuous and at first glance would be thought to be certain metal lines. Despite exhaustive searches, this conclusion cannot be verified.